

# Proposed Five-Electron Charge Quadrupole Qubit

John H. Caporaletti and J. P. Kestner

*Department of Physics, University of Maryland Baltimore County, Baltimore, MD 21250, USA*

A charge qubit couples to environmental electric field fluctuations through its dipole moment, resulting in fast decoherence. We propose the  $p$  orbital ( $pO$ ) qubit, formed by the single electron,  $p$ -like valence states of a five-electron Si quantum dot, which couples to charge noise through the *quadrupole* moment. We demonstrate that the  $pO$  qubit offers distinct advantages in quality factor, gate speed, readout and size. We use a phenomenological, dipole two-level-fluctuator charge noise model to estimate a  $T_2^* \sim 80$  ns. In conjunction with Rabi frequencies of order 10 GHz, an order of magnitude improvement in qubit quality factor is expected relative to state-of-the-art semiconductor spin qubits. The  $pO$  qubit features all-electrical control via modulating the dot's eccentricity. We also show how to perform two-qubit gates via the  $1/r^5$  quadrupole-quadrupole interaction. We find a universal gate set using gradient ascent based control pulse optimization, subject to 10 GHz maximum allowable bandwidth and 1 ns pulse times.

Using qubits to manipulate information fundamentally differs from classical computing schemes and offers potential advantages depending on the computational problem being solved [1–3]. Many candidate qubit systems exist, such as semiconductor, trapped ion, superconducting, topological, and photonic qubits. Each candidate has unique strengths and weaknesses, populating a high-dimensional parameter space with axes such as size, coherence time, gate speed, scalability, addressability, experimental feasibility, etc. In this work we add a new candidate that prioritizes size and the product of coherence time and gate speed (i.e., quality factor), a quantum dot charge qubit we will refer to as the  $p$  orbital ( $pO$ ) qubit since it is formed via the  $p$  orbital subspace.

The first realization of a semiconductor charge qubit consisted of a double quantum dot containing a single electron [4, 5], with logical states being left  $|L\rangle$  or right  $|R\rangle$  dot occupancy. The key feature of this qubit is its large dipole moment between  $|L\rangle$  and  $|R\rangle$ , so it is sometimes referred to as a “charge dipole” (CD) qubit [6]. Accordingly, the CD qubit is strongly coupled to the electric field and therefore has fast gate operations but also fast decoherence. To circumvent decoherence, the CD qubit can be parked at a ‘sweet spot’ corresponding to zero detuning between dot chemical potentials [7], but performing nontrivial gates requires moving the qubit away from the sweet spot. The quality factor, defined as the product of the Rabi frequency and the  $T_2^*$  dephasing time, for a CD qubit is generally worse than for a spin qubit [8]. For this reason, research on semiconductor based qubits in the last 15 years has been dominated by the spin degree of freedom (DOF).

However, a recent proposal, called the charge quadrupole qubit [6, 9–11], moves past the ‘sweet spot’ idea by having no dipole moment between its basis states at *any* operating point. Its coupling to the electric field is always via the quadrupole moment, although this beneficial structuring of the interaction with the environment is at the expense of adding a third dot to the qubit footprint and introducing a low-lying leakage state.

Earlier work has also noted the benefit of working with higher-multipole based charge qubits using multiple dots [12, 13]. The  $pO$  qubit, on the other hand, achieves this quadrupole structure with only a single dot and no leakage state. In this sense, the  $pO$  qubit marks a distinct evolution of the charge qubit.

In this letter, we first present the system Hamiltonian, validate significant assumptions about our model, and discuss single-qubit control. Second, in an effort to quantify the  $pO$  qubits performance, we use a dipole two-level fluctuator (TLF) model to estimate the  $pO$  qubit’s inhomogeneous dephasing time and gate infidelities. We use the same model to estimate corresponding quantities for state-of-the-art semiconductor based qubits in order to draw a fair comparison. Third, we find a universal set of gates via pulse optimization for two neighboring  $pO$  qubits with an always-on quadrupole-quadrupole Coulomb interaction. Finally, we show that readout/initialization can be carried out using a quantum point contact to measure along the  $x$  or  $y$  axes of the Bloch sphere.

Consider a laterally defined quantum dot in a semiconductor heterostructure with an out-of-plane magnetic field of magnitude  $B_z$ . Modeling the dot as an isotropic 2D harmonic oscillator, the Hamiltonian governing an electron’s orbital dynamics is

$$H_0 = \frac{(-i\hbar\nabla + e\mathbf{A})^2}{2m^*} + \frac{e}{2}m^*\omega_0^2r^2, \quad (1)$$

where the symmetric gauge is chosen,  $\mathbf{A} = \frac{B_z}{2}(-y\hat{\mathbf{x}} + x\hat{\mathbf{y}})$ , yielding  $\mathbf{B} = B_z\hat{\mathbf{z}}$ . Additionally,  $r$  is the radial position operator,  $\omega_0$  is the confinement frequency,  $m^*$  is the effective mass and  $e$  is the electron’s charge. Solving the corresponding Schrödinger equation for Eq. (1) yields

the Fock-Darwin states [14],[15]

$$\psi_{n,m}(x,y) = \frac{1}{l_0} \sqrt{\frac{\left(\frac{n-|m|}{2}\right)!}{\pi \left(\frac{n+|m|}{2}\right)!}} \left(\frac{x + iy \text{sgn}(m)}{l_0}\right)^{|m|} \times e^{-\frac{x^2+y^2}{2l_0^2}} L_{\frac{n-|m|}{2}}^{|m|}\left(\frac{x^2+y^2}{2l_0^2}\right), \quad (2)$$

where  $l_0 = l_B/(\frac{1}{4} + \frac{\omega_0^2}{\omega_c^2})^{\frac{1}{4}}$ ,  $l_B = \sqrt{\hbar/m^*\omega_c}$ , and  $\omega_c = eB_z/m^*$  are the dot's characteristic length, magnetic length and cyclotron angular frequency respectively.  $L_b^a(x)$  is the associated Laguerre polynomials,  $n \in \mathbb{Z}_0^+$ , and  $m = -n, -n+2, \dots, n-2, n$ . The energy spectrum is

$$E_{n,m} = (n+1)\hbar\omega_c \sqrt{\frac{1}{4} + \frac{\omega_0^2}{\omega_c^2}} + m\frac{\hbar}{2}\omega_c. \quad (3)$$

In analogy with the hydrogen atom,  $n=0$  is referred to as the  $s$  orbital,  $n=1$  as the  $p$  orbitals and so on. Specifically,  $\psi_{1,m}(x,y) = \langle x,y|p_m\rangle$  and  $\{|p_{+1}\rangle, |p_{-1}\rangle\}$  spans a two-dimensional subspace that is energetically isolated from the  $s$  and  $d$  orbital states by the orbital level spacing, given that  $\omega_0 \gg \omega_c$ .

In order to have an electron stably occupy the  $p$  orbital, one must fill the  $s$  orbital such that orbital decays are Pauli blocked. In the case of Si, the electron has both spin and valley DOFs along with charge. So, one needs four electrons to fill the four  $s$  spin-orbital states, and a fifth electron to reside in the  $p$  orbital. This idea of a 'frozen core' [16–18] approximates the intra-dot e-e interactions as a renormalization to the dot potential size, generally not affecting the  $p$  orbital's characteristic shape, and the intuitive idea has experimental support [19].

Qubit operations within this subspace can be performed via deformations of the dot, similar to the case of a spin-charge qubit [20]. Consider a deforming potential operator,  $V_d$ , expanded about the center of the dot,

$$V_d \approx V_d|_0 + (\partial_i V_d)|_0 r_i + \frac{1}{2}(\partial_j \partial_k V_d)|_0 r_j r_k, \quad (4)$$

where  $r_a \in \{x, y\}$ ,  $\partial_a \in \{\partial_x, \partial_y\}$  and repeated indices are summed over. Writing the corresponding deformation Hamiltonian in the  $|p_m\rangle$  basis yields

$$H_d = eV_d \approx \frac{el_0^2}{4}((\partial_x^2 - \partial_y^2)V_d|_0 \sigma_x + 2\partial_x \partial_y V_d|_0 \sigma_y) = \frac{\hbar}{2}(\Omega_x \sigma_x + \Omega_y \sigma_y), \quad (5)$$

where  $\sigma_i$  are the Pauli operators in this basis. The monopole and dipole term of Eq. (4) contribute identity and zero respectively. Therefore, the deforming Hamiltonian is dictated, to leading order, by the quadrupole terms shown in Eq. (5). Each term can be interpreted

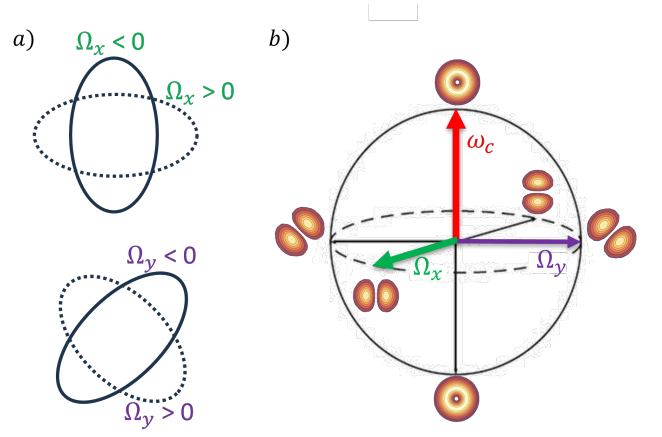


FIG. 1. a) Various potential deformations and the resulting types of rotations. b) Depiction of qubit control. For six of the Bloch sphere's antipodes, the corresponding charge distribution of the  $pO$  qubit is shown.

as a difference in confinement frequencies along a pair of orthogonal spatial axes of the dot (the two sets differing by an angle of  $\pi/4$ ) as shown in Fig. 1a).

The single-qubit  $pO$  Hamiltonian in the  $|p_m\rangle$  basis is thus

$$H_{1q} = H_0 + H_d = \frac{\hbar}{2}(\Omega_x \sigma_x + \Omega_y \sigma_y + \omega_c \sigma_z), \quad (6)$$

with  $\Omega_x, \Omega_y, \omega_c \in \mathbb{R}$ . A graphical depiction of Eq. (6) on the Bloch sphere is shown in Fig. 1b). Only two of the three axes in Eq. (6) are required to span  $\mathfrak{su}(2)$ . If  $\omega_c \neq 0$ , one type of deformation suffices. If  $\omega_c = 0$ , independent control over  $\Omega_x$  and  $\Omega_y$  is required. A gate electrode architecture such as the crossbar design developed in [21, 22] is sufficient for this. Controllable dot anisotropies have been demonstrated corresponding to a difference in confinement energies along orthogonal axes of order  $100\mu\text{eV}$  [19], implying that  $\Omega_i$  can be tuned from zero (for an isotropic dot) up to a magnitude of  $2\pi \times 25$  GHz. For a dot size of  $l_0 = 10$  nm (which we take henceforth), this corresponds to a deformation in dot size of  $\sim 1\%$ .

The rapid control speed is a result of the  $pO$  qubit's coupling to the electric field, but this also facilitates decoherence. However, the coupling is now via the quadrupole moment to second derivatives of the electric potential instead of via the dipole moment to first derivatives of the electric potential. We expect that as the order to which the qubit couples increases, our ability to artificially induce these structured changes in the environment (e.g., deforming the dots instead of simply detuning them relative to each other) will increasingly exceed the natural level of fluctuations at that order. To demonstrate this, and compare our qubits decoherence to the state-of-the-art, we now use a phenomenological model of charge noise.

For simplicity, and to establish an upper bound on the  $pO$  qubit's decoherence, only inhomogeneous dephasing will be considered, as estimated by [5, 23, 24]

$$T_2^* = \frac{\sqrt{2}\hbar}{\sigma_E}, \quad (7)$$

where  $\sigma_E = \sqrt{\langle E^2 \rangle - \langle E \rangle^2}$  with  $E$  being the energy splitting between eigenstates of the system's full Hamiltonian, including noise, and  $\langle \cdot \rangle$  denoting an ensemble average.

Charge noise is suspected to originate from an ensemble of TLFs [25]. Recent work suggests that the TLFs consist of electric dipoles at, and oriented parallel to, the interface between the heterostructure and the electrodes [26]. This ensemble of dipoles produces a potential  $V_{\text{noise}}(x, y)$  at the dot, producing an additional uncontrolled source of deformation in Eq. (5). The energy splitting  $E$  is

$$E = \sqrt{|H_{1q} + eV_{\text{noise}}|^2} \\ = \hbar \sqrt{(\Omega_x + \delta\Omega_x)^2 + (\Omega_y + \delta\Omega_y)^2 + \omega_c^2} \quad (8)$$

where  $\|A\| = \sqrt{\text{Tr}(AA^\dagger)}$ . We perform several Monte Carlo simulations with the parameters given in Table I to obtain an estimate of  $T_2^* \approx 80$  ns [27]. All simulations use  $\omega_c = 0$ , as this is when the  $pO$  qubit is most vulnerable to charge noise while idling.

Parameter	Symbol	Value
Dipole Length	$d$	.1 nm [28]
Dot Distance to Electrodes	$D$	100 nm
Characteristic Dot Length	$l_0$	10 nm
Dipole Density	$\rho$	$10^{-3}\text{nm}^{-2}$ [29]
Interface Area	$A$	$10^4\text{nm}^2$

TABLE I. Noise model parameters. Note that  $\rho$  is uniform.

The above only accounts for charge noise coupling to the quadrupole moment. There can also be dephasing due to magnetic Overhauser noise and higher order electric coupling. The magnetic coupling of the  $pO$  qubit differs from a typical Loss-DiVincenzo (LD) style qubit [30] because the orbital gyromagnetic ratio features the effective electron mass in Si while the spin gyromagnetic ratio uses the intrinsic electron mass. Consequently, the magnetic dephasing of a  $pO$  qubit is proportional to that of an LD qubit,  $T_2^* = \frac{gm^*}{2m_e} T_2^{*(LD)}$ , where  $g$  is the electron  $g$  factor and  $m_e$  is the bare electron mass. Using the inhomogeneous dephasing time of an LD qubit in isotopically enriched silicon  $T_2^{*(LD)} = 33\mu\text{s}$  [31] and  $m^* = 0.19m_e$  [32], the  $pO$  magnetic dephasing time is  $\approx 6\mu\text{s}$ . Therefore, Overhauser noise is not the limiting factor in dephasing and can safely be neglected.

As for higher order electric noise, the  $pO$  qubit does not have any coupling to odd spatial derivatives of the potential about the dot because the  $p$  orbitals are symmetric about the origin. Therefore, to find corrections

to our model, one must look past the octupole term to the hexadecapole term, which couples to the  $4^{\text{th}}$  order derivatives of  $V_{\text{noise}}$ . Assuming the potential produced by a single point dipole, the ratio between the quadrupole and  $n^{\text{th}}$  term in the Taylor expansion of Eq. (4) goes like  $\sim (l_0/D)^{n-2}$  after averaging over all possible dipole locations and orientations in  $A$ . The hexadecapole to quadrupole ratio is then  $\sim 10^{-2}$  for the parameters in Table I. Therefore, higher order electric couplings can be safely ignored.

One of the simplest ways to quantify a qubit's performance is the quality factor, given by

$$Q = f_R T_2^*, \quad (9)$$

where  $f_R$  is the Rabi frequency accessible to the qubit. This definition is in accordance with the *qubit* quality factor in Ref. [33] and represents an intrinsic qubit quality, i.e., in the absence of any dynamical decoupling. (This is in contrast to the *gate* quality factor, which measures dephasing when driving on an axis orthogonal to the quantization axis.) Assuming the validity of the TLF ensemble noise model, we predict the  $pO$  qubit to have  $Q \approx 1000$ .

Furthermore, the highest semiconductor single-qubit quality factor we know of is for an LD spin qubit controlled via electric dipole spin resonance (EDSR) with  $Q = 78$  [34]. We again apply our noise model to a straightforward model of the LD spin qubit using the reported parameters of Ref. [34]. Details can be found in the Supplemental Material [27]. The only free parameter in our calculation is the confinement energy  $\hbar\omega_0$  of the LD qubit dot, and we obtain Ref. [34]'s experimentally observed value of  $T_2^* \approx 20\mu\text{s}$  by taking a value  $\hbar\omega_0 \approx 2$  meV, in agreement with the order of magnitude estimation in Ref. [34]. Using their estimate  $\hbar\omega_0 = 1$  meV directly without any fitting predicts a shorter dephasing time of  $\sim 5\mu\text{s}$ . So, if anything, we are overestimating the amount of noise the  $pO$  qubit will see, and its qubit quality factor is likely to indeed be an order-of-magnitude larger than the state-of-the-art spin qubits.

We also want multi-qubit interactions to allow for the entangling operations that are at the heart of quantum computing. Consider two adjacent quantum dots, modeled by a symmetric, bi-quadratic well whose centers lie at  $x = \pm \frac{L}{2}$ . In the limit that  $L \gg l_0$ , the single particle orbital states remain harmonic oscillator states,

$$\psi_{1,m}^\pm(x, y) = \langle x, y | p_m^\pm \rangle = e^{\pm i \frac{L y}{4 l_0}} \psi_{1,m}(x \pm \frac{L}{2}, y), \quad (10)$$

where the  $+$ ( $-$ ) sign corresponds to occupancy of the left (right) dot. The phase factor is the result of a gauge transformation when redefining the coordinate system's origin to be mid-way between dots, and vanishes in the absence of a magnetic field [18].

Although the complete two-electron state must be antisymmetric, we will consider distances of  $L$  such

that wavefunction overlap produces negligible kinetic exchange [27] compared to the Coulomb interaction. Kinetic exchange is undesirable because its strength depends on both the joint spin state and orbital state of both electrons, thus coupling the spin and orbit DOFs and ultimately producing decoherence in the  $p$  orbital space. When such wavefunction overlap is negligible, we can treat electrons in each dot as distinguishable. Therefore, the two particle charge basis states subsequently used are

$$|m, m'\rangle = |p_m^+\rangle_1 \otimes |p_{m'}^-\rangle_2, \quad (11)$$

where the subscripts 1 and 2 distinguish the electrons.

The Coulomb operator is given by

$$H_c = \frac{e^2}{4\pi\epsilon_0\epsilon_r} \frac{1}{|\vec{r}_1 - \vec{r}_2|}, \quad (12)$$

where  $\vec{r}_i$  is the position operator for the  $i^{\text{th}}$  electron. Writing  $H_c$  in the basis states of Eq. (11) for two qubits a distance  $L$  apart, Eq. (12) becomes

$$H_c = \frac{\hbar}{2} \left( \Omega_{xx} \sigma_x^{(1)} \sigma_x^{(2)} + \Omega_{yy} \sigma_y^{(1)} \sigma_y^{(2)} + a \left( \sigma_x^{(1)} + \sigma_x^{(2)} \right) \right) \quad (13)$$

where  $\Omega_{xx}$  and  $\Omega_{yy}$  are the two-qubit quadrupole-quadrupole Coulomb interaction strengths,  $a$  is the single-qubit effect of deformation of one dot due to the charge monopole of the other, and the superscripts denote which part of the tensor space the Pauli operators act on.  $\Omega_{xx}$  and  $\Omega_{yy}$  are opposite in sign and shown in Fig. 2. For the domain of Fig. 2,  $a$  ranges from ap-

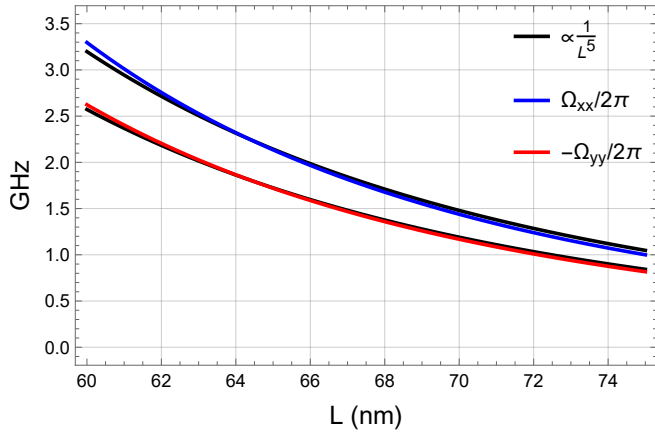


FIG. 2. Plot of two-qubit interaction strengths as a function of inter-dot distance  $L$ .  $\frac{1}{L^5}$  fit is shown in black for both  $\Omega_{xx}$  and  $\Omega_{yy}$ .

proximately 5 – 20 GHz, effectively skewing the origin of  $\Omega_x^{(1),(2)}$ . However, this effect would be calibrated away in the initial setup of the device. No  $\sigma_z$  terms are present in Eq. (13) because the Coulomb operator cannot distinguish between the identical charge distributions of  $|p_{\pm}\rangle$ .

Additionally, the term  $\sigma_x \sigma_y$  is not present because the  $\sigma_x$  eigenstates,  $|p_{x,y}\rangle$ , do not produce a difference in curvature along the two axes  $\hat{x} + \hat{y}$  and  $\hat{x} - \hat{y}$ . The full Hamiltonian, combining both local and interaction energies, becomes

$$H_{2q} = \sum_{k=1}^2 \frac{\hbar}{2} \left( \Omega_x^{(k)} \sigma_x^{(k)} + \Omega_y^{(k)} \sigma_y^{(k)} + \omega_c \sigma_z^{(k)} \right) + \frac{\hbar}{2} \Omega_{xx} \sigma_x^{(1)} \sigma_x^{(2)} + \frac{\hbar}{2} \Omega_{yy} \sigma_y^{(1)} \sigma_y^{(2)}. \quad (14)$$

With the always-on Coulomb interaction in Eq. (14), it is not obvious how single-qubit gates should be performed. By means of gradient ascent pulse engineering (GRAPE) [35], we search the space of possible pulses for qubit unitaries within the set  $\{H^{(k)}, S^{(k)}, T^{(k)}, bSWAP\}$ , where  $H^{(k)}$  is the Hadamard gate on qubit  $k$ , and likewise  $S^{(k)}$  and  $T^{(k)}$  are phase gates of angle  $\frac{\pi}{2}$  and  $\frac{\pi}{4}$  respectively, while  $bSWAP$  is a maximally entangling gate that is naturally generated by  $\sigma_x^{(1)} \sigma_x^{(2)} - \sigma_y^{(1)} \sigma_y^{(2)}$  and is equivalent to  $iSWAP$  up to local operations. The pulse control parameters are given by the set  $C = \{\Omega_x^{(1)}, \Omega_y^{(1)}, \Omega_x^{(2)}, \Omega_y^{(2)}\}$ . Pulses for each element of the universal gate set are found for  $\omega_c \neq 0$  and  $\omega_c = 0$  and shown in the Supplementary Material [27]. Gate times are 1 ns for all pulses with system parameters  $L = 63$  nm, corresponding to  $\Omega_{xx} \approx 2.5$  GHz and  $\Omega_{yy} \approx -2.0$  GHz. Our choice of  $L$  is large enough that  $\Omega_{xx,yy}$  is more than  $100\times$  greater than kinetic exchange, as assumed in Eq. (11), but the two dots are still near enough that  $\Omega_{xx,yy} \sim \Omega_{x,y}$  so two-qubit gates can be performed on the same timescale as single-qubit gates. The approximate range of  $L$  which satisfies these requirements is  $60 \lesssim L \lesssim 75$  nm. The pulses assume an available bandwidth of at most 10 GHz, which is the state of the art for AWGs [36]. Similar optimizations could also be performed for less advanced AWGs as necessary.

For each gate in the universal gate set, we again perform Monte Carlo noise simulations using the parameters in Table I, taking into account both single-qubit noise (i.e., fluctuations in eccentricity, causing noise in  $\Omega_x$  and  $\Omega_y$ ) and two-qubit noise (i.e., fluctuations in the inter-dot distance  $L$ , causing noise in  $\Omega_{xx}$  and  $\Omega_{yy}$ ). However, for  $L = 63$  nm and  $l_0 = 10$  nm, single-qubit noise is the limiting factor. Infidelities are found to be of order  $10^{-5} - 10^{-4}$  for all gates [27].

We now consider initialization and readout for the  $pO$  qubit. Recognizing that the eigenstates of  $\sigma_x$ ,  $|p_{x,y}\rangle$ , have different charge configurations (see Fig. 1a), it is possible to perform readout on the qubit state without the selective tunneling typically used in Elzerman readout [37] or Pauli spin blockade [38]. Different voltages are produced by  $|p_x\rangle$  and  $|p_y\rangle$  at a device such as a quantum point contact (QPC) nearby. This corresponds to a chemical potential difference at the QPC and can be extracted using current measurements, as in Refs. [26, 39]. For

charge noise with a power spectral density  $S = \frac{A}{f}$  and  $A \sim 1 \mu\text{eV}^2$  [26, 39–42], we calculate the signal-to-noise ratio (SNR) as a function of QPC-to-qubit distance  $x_p$  and measurement time  $t_m$ ,

$$\text{SNR} = \frac{\langle V \rangle}{\sigma_V}, \quad (15)$$

where  $V = \int_0^{t_m} dt V(t)$ ,  $V(t)$  is the measured voltage at the QPC as a function of time. Fig. 3 shows that the  $pO$  qubit offers rapid readout.

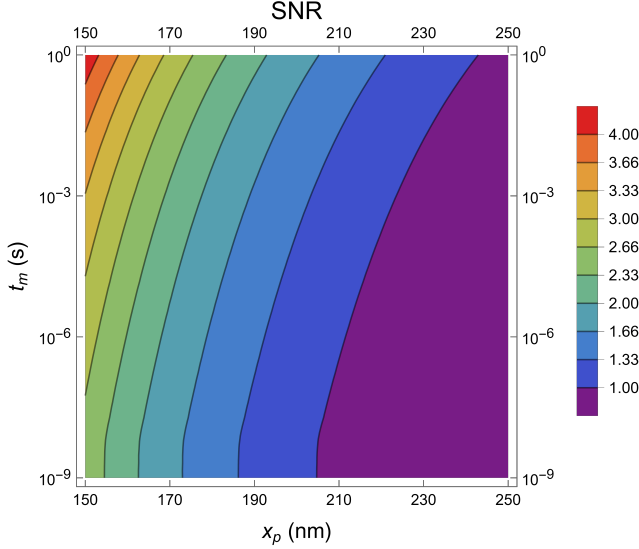


FIG. 3. Signal-to-noise ratio as a function of QPC-to-qubit distance ( $x_p$ ) and measurement time ( $t_m$ ).

In summary, we propose a charge qubit that makes use of the two-level  $p$  orbital subspace in a five-electron silicon quantum dot. We found an all-electrical, universal gate set with 1 ns gate times, with similarly fast readout, and even faster gate speeds  $\sim 100$  ps are feasible if one has fast enough classical control electronics. We estimate an inhomogeneous dephasing time of the  $pO$  qubit of  $T_2^* \approx 80$  ns, implying a single-qubit quality factor of  $Q \sim 1000$ . Looking forward, the  $pO$  qubit appears to be a strong direction for future research because it requires only a single dot, with no low-lying leakage states, and electric control. Future work will consider controlling a scalable array of  $pO$  qubits.

The authors acknowledge support from the Army Research Office (ARO) under Grant Number W911NF-23-1-0115.

- (Association for Computing Machinery, New York, NY, USA, 1996) p. 212–219.
- [3] A. Peruzzo, J. McClean, P. Shadbolt, M.-H. Yung, X.-Q. Zhou, P. J. Love, A. Aspuru-Guzik, and J. L. O’Brien, *Nat. Commun.* **5**, 4213 (2014).
  - [4] J. Gorman, D. G. Hasko, and D. A. Williams, *Phys. Rev. Lett.* **95**, 090502 (2005).
  - [5] K. D. Petersson, J. R. Petta, H. Lu, and A. C. Gossard, *Phys. Rev. Lett.* **105**, 246804 (2010).
  - [6] M. Friesen, J. Ghosh, M. A. Eriksson, and S. N. Coppersmith, *Nat. Commun.* **8**, 15923 (2017).
  - [7] D. Kim, D. R. Ward, C. B. Simmons, J. K. Gamble, R. Blume-Kohout, E. Nielsen, D. E. Savage, M. G. Lagally, M. Friesen, S. N. Coppersmith, and M. A. Eriksson, *Nature Nanotech.* **10**, 243 (2015).
  - [8] P. Stano and D. Loss, *Nat. Rev. Phys.* **4**, 672 (2022).
  - [9] V. Kornich, M. G. Vavilov, M. Friesen, and S. N. Coppersmith, *New J. Phys.* **20**, 103048 (2018).
  - [10] J. V. Koski, A. J. Landig, M. Russ, J. C. Abadillo-Uriel, P. Scarlino, B. Kratochwil, C. Reichl, W. Wegscheider, G. Burkard, M. Friesen, S. N. Coppersmith, A. Wallraff, K. Ensslin, and T. Ihn, *Nat. Phys.* **16**, 642 (2020).
  - [11] B. Kratochwil, J. V. Koski, A. J. Landig, P. Scarlino, J. C. Abadillo-Uriel, C. Reichl, S. N. Coppersmith, W. Wegscheider, M. Friesen, A. Wallraff, T. Ihn, and K. Ensslin, *Phys. Rev. Res.* **3**, 013171 (2021).
  - [12] D. K. L. Oi, S. G. Schirmer, A. D. Greentree, and T. M. Stace, *Phys. Rev. B* **72**, 075348 (2005).
  - [13] M. Hentschel, D. C. B. Valente, E. R. Mucciolo, and H. U. Baranger, *Phys. Rev. B* **76**, 235309 (2007).
  - [14] V. Fock, *Z. Phys.* **47**, 446 (1928).
  - [15] C. G. Darwin, *Proc. R. Soc. Lond. A* **117**, 258 (1927).
  - [16] E. S. Sachs, J. Hinze, and N. H. Sabelli, *J. Chem. Phys.* **62**, 3393 (1975).
  - [17] X. Hu and S. Das Sarma, *Phys. Rev. A* **64**, 042312 (2001).
  - [18] E. Barnes, J. P. Kestner, N. T. T. Nguyen, and S. Das Sarma, *Phys. Rev. B* **84**, 235309 (2011).
  - [19] R. C. C. Leon, C. H. Yang, J. C. C. Hwang, J. C. Lemyre, T. Tanttu, W. Huang, K. W. Chan, K. Y. Tan, F. E. Hudson, K. M. Itoh, A. Morello, A. Laucht, M. Pioro-Ladrière, A. Saraiva, and A. S. Dzurak, *Nat. Commun.* **11**, 797 (2020).
  - [20] J. Kyriakidis and G. Burkard, *Phys. Rev. B* **75**, 115324 (2007).
  - [21] R. Li, L. Petit, D. P. Franke, J. P. Dehollain, J. Helsen, M. Steudtner, N. K. Thomas, Z. R. Yoscovits, K. J. Singh, S. Wehner, L. M. K. Vandersypen, J. S. Clarke, and M. Veldhorst, *Sci. Adv.* **4**, eaar3960 (2018).
  - [22] F. Borsoi, N. W. Hendrickx, V. John, M. Meyer, S. Motz, F. van Riggelen, A. Sammak, S. L. de Snoo, G. Scappucci, and M. Veldhorst, *Nature Nanotech.* **19**, 21 (2024).
  - [23] R. Kubo, *J. Phys. Soc. Jpn.* **9**, 935 (1954).
  - [24] E. Kawakami, P. Scarlino, D. R. Ward, F. R. Braakman, D. E. Savage, M. G. Lagally, M. Friesen, S. N. Coppersmith, M. A. Eriksson, and L. M. K. Vandersypen, *Nature Nanotech.* **9**, 666 (2014).
  - [25] A. V. Kuhlmann, J. Houel, A. Ludwig, L. Greuter, D. Reuter, A. D. Wieck, M. Poggio, and R. J. Warburton, *Nat. Phys.* **9**, 570 (2013).
  - [26] E. J. Connors, J. J. Nelson, H. Qiao, L. F. Edge, and J. M. Nichol, *Phys. Rev. B* **100**, 165305 (2019).
  - [27] Publisher to insert link.
  - [28] J. Reinisch and A. Heuer, *J. Phys. Chem. B* **110**, 19044 (2006).

- [1] P. Shor, in *Proceedings 35th Annual Symposium on Foundations of Computer Science* (1994) pp. 124–134.
- [2] L. K. Grover, in *Proceedings of the Twenty-Eighth Annual ACM Symposium on Theory of Computing*, STOC ’96

- [29] J. Zimmermann and G. Weber, Phys. Rev. Lett. **46**, 661 (1981).
- [30] D. Loss and D. P. DiVincenzo, Phys. Rev. A **57**, 120 (1998).
- [31] K. W. Chan, W. Huang, C. H. Yang, J. C. C. Hwang, B. Hensen, T. Tanttu, F. E. Hudson, K. M. Itoh, A. Laucht, A. Morello, and A. S. Dzurak, Phys. Rev. Appl. **10**, 044017 (2018).
- [32] G. Burkard, T. D. Ladd, A. Pan, J. M. Nichol, and J. R. Petta, Rev. Mod. Phys. **95**, 025003 (2023).
- [33] P. Stano and D. Loss, Nat. Rev. Phys. **4**, 672 (2022).
- [34] J. Yoneda, K. Takeda, T. Otsuka, T. Nakajima, M. R. Delbecq, G. Allison, T. Honda, T. Koder, S. Oda, Y. Hoshi, N. Usami, K. M. Itoh, and S. Tarucha, Nature Nanotech. **13**, 102 (2018).
- [35] N. Khaneja, T. Reiss, C. Kehlet, T. Schulte-Herbrüggen, and S. J. Glaser, J. Magn. Reson. **172**, 296 (2005).
- [36] D. Kim, Z. Shi, C. B. Simmons, D. R. Ward, J. R. Prance, T. S. Koh, J. K. Gamble, D. E. Savage, M. G. Lagally, M. Friesen, S. N. Coppersmith, and M. A. Eriksson, Nature **511**, 70 (2014).
- [37] J. M. Elzerman, R. Hanson, L. H. Willems van Beveren, B. Witkamp, L. M. K. Vandersypen, and L. P. Kouwenhoven, Nature **430**, 431 (2004).
- [38] N. S. Lai, W. H. Lim, C. H. Yang, F. A. Zwanenburg, W. A. Coish, F. Qassemi, A. Morello, and A. S. Dzurak, Sci. Rep. **1**, 110 (2011).
- [39] B. Paquelet Wuetz, D. Degli Esposti, A.-M. J. Zwerver, S. V. Amitonov, M. Botifoll, J. Arbiol, A. Sammak, L. M. K. Vandersypen, M. Russ, and G. Scappucci, Nat. Commun. **14**, 1385 (2023).
- [40] E. J. Connors, J. Nelson, L. F. Edge, and J. M. Nichol, Nat. Commun. **13**, 940 (2022).
- [41] B. M. Freeman, J. S. Schoenfield, and H. Jiang, Appl. Phys. Lett. **108**, 253108 (2016).
- [42] T. Struck, A. Hollmann, F. Schauer, O. Fedorets, A. Schmidbauer, K. Sawano, H. Riemann, N. V. Abrosimov, Ł. Cywiński, D. Bougeard, and L. R. Schreiber, npj Quantum Inf. **6**, 40 (2020).

## Supplemental Material

### I. MONTE CARLO

We estimate  $T_2^*$  via a Monte Carlo noise simulation. We model the noise source as  $n = \rho A$  dipoles at the heterostructure interface and oriented parallel to it. First, the center of mass position  $(x_i, y_i)$  and in-plane orientation  $(\phi_i)$  of the dipoles are randomly and uniformly generated over the intervals  $\{x_i, y_i \in \mathbb{R} | -\frac{\sqrt{A}}{2} < x_i, y_i < \frac{\sqrt{A}}{2}\}$  and  $\{\phi_i \in \mathbb{R} | 0 < \phi_i < 2\pi\}$ . This randomly selects a single configuration of dipoles out of the ensemble of possible configurations, defining a particular, random noise potential instance. Then we calculate  $\delta\Omega_x$  and  $\delta\Omega_y$  by taking second derivatives of the potential instance at the dot and put these into Eq. (8) to obtain the fluctuation in the energy splitting. Repeating this process  $N$  times, we generate a distribution of energy splittings, from which we obtain a standard deviation  $\sigma_E$  and hence, from Eq. (7),  $T_2^*$ .

$T_2^*$  times reported in the main text represent a mean  $T_2^*$  time for 100 Monte Carlo simulations with  $N = 1000$ , as indicated in Fig. S1.

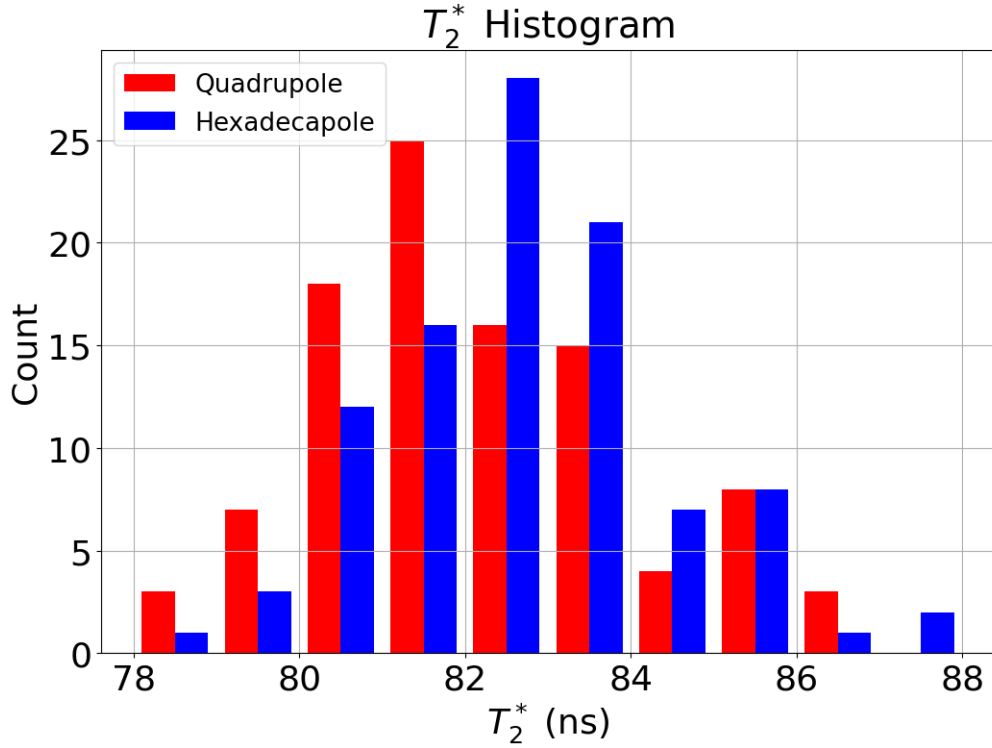


FIG. S1. Two  $T_2^*$  distributions plotted simultaneously. Red data corresponds to the noise potential truncated at the quadrupole order, while the blue is truncated at the hexadecapole order.

Monte Carlo simulations are also used to calculate the average gate infidelity of the pulses shown in Fig. S2. Fluctuations in two-qubit parameters  $(\Omega_{xx}, \Omega_{yy})$  must now be captured along with single-qubit parameters  $(\Omega_x^{(1)}, \Omega_y^{(1)}, \Omega_x^{(2)}, \Omega_y^{(2)}, a)$ . Fluctuations in the two-qubit terms arise due to fluctuations of the interdot distance  $L$ , given by  $\delta L = \delta r^{(1)} - \delta r^{(2)}$ , where the  $i^{th}$  dot's shift is given by

$$\delta r^{(i)} = \frac{e}{m^* \omega_0^2} \delta F^{(i)}, \quad (S1)$$

and  $\delta F^{(i)}$  is the local electric field fluctuation at the  $i^{th}$  dot.  $L$  is less sensitive to motion orthogonal to the connecting axis between dots than parallel motion. Therefore, only parallel fluctuations in  $L$  are calculated in the Monte Carlo simulation and  $\delta F^{(i)}/\delta r^{(i)}$  can be considered scalars. Fluctuations in  $(\Omega_{xx}, \Omega_{yy}, a)$  are different from the other parameters because they originate from  $\delta L$ . We calculate their fluctuations simply as  $\delta\Omega_{xx} \approx \frac{d\Omega_{xx}}{dL} \delta L$ ,  $\delta\Omega_{yy} \approx \frac{d\Omega_{yy}}{dL} \delta L$ , and  $\delta a \approx \frac{da}{dL} \delta L$ , assuming  $\delta L$  is small.



The Monte Carlo procedure for calculating pulse infidelities again begins by randomly sampling the configuration space of dipole locations. This produces perturbations  $(\delta\Omega_x^{(1)}, \delta\Omega_y^{(1)}, \delta\Omega_x^{(2)}, \delta\Omega_y^{(2)}, \delta\Omega_{xx}, \delta\Omega_{yy})$  through the first and second derivatives of the noise potential instance at both dots. We compute the unitary evolution due to each perturbed pulse and evaluate the infidelity. This process is repeated  $N$  times, after which we average each pulse's infidelity.

The result of a single Monte Carlo simulation with  $N = 1000$  predicts the pulse infidelities in Table I. Generally, gates with  $B \neq 0$  have less infidelity because those pulses require less control parameters affected by charge noise.

Gate	$f_c = 4.5$ GHz	$f_c = 0$ GHz
bSWAP	0.6	1
HI	0.6	6
TI	0.5	3
SI	0.9	3
II	0.4	2

TABLE I. Values of average infidelity  $\langle 1 - \mathcal{F} \rangle \times 10^{-5}$  for all eight GRAPE optimized pulses in the presence of single and two qubit noise.

## II. ANALYTICAL NOISE CALCULATIONS

For a given dipole configuration, the standard deviation (SD) of voltage  $\sigma_V$  and electric field  $\sigma_F$  can be calculated exactly. Consider a point dipole whose center of mass coordinates are  $(x_i, y_i, h)$ , with a dipole vector parallel to the  $z = h$  plane. The angle made by the dipole vector and the  $x$  axis is  $\phi_i$ . The potential produced by the dipole at the point  $(x, y, 0)$  is given by

$$V_{dip}(\vec{r}, \vec{r}_i, \phi_i) = \frac{qd}{4\pi\epsilon_r\epsilon_0} \frac{(x - x_i)\cos(\phi_i) + (y - y_i)\sin(\phi_i)}{((x - x_i)^2 + (y - y_i)^2 + h^2)^{3/2}} \quad (S2)$$

where  $q$  is the charge of the dipole and  $d$  is the dipole length. The entire noise potential, for  $n$  dipoles, is given by

$$V(\vec{r}, \vec{r}_1, \dots, \vec{r}_n) = \sum_{i=1}^n V_{dip}(\vec{r}, \vec{r}_i, \phi_i) \quad (S3)$$

The SD of the potential can be calculated by the following equation

$$\sigma_V^2 = \langle V^2 \rangle - \langle V \rangle^2 = \frac{1}{(2\pi)^n A^n} \prod_{j=1}^n \iint_A dA_j \int_0^{2\pi} d\phi_j V(\vec{r}, \vec{r}_1, \dots, \vec{r}_n)^2 - \left( \frac{1}{(2\pi)^n A^n} \prod_{i=j}^n \iint_A dA_j \int_0^{2\pi} d\phi_j V(\vec{r}, \vec{r}_1, \dots, \vec{r}_n) \right)^2. \quad (S4)$$

Integrating first over the  $\phi$  variables,  $\langle V^2 \rangle$  has inter-dipole cross terms that integrate to zero while  $\langle V \rangle^2$  vanishes entirely. We are left with

$$\begin{aligned} \sigma_V^2 &= \frac{1}{(2\pi)^n A^n} \prod_{j=1}^n \iint_A dA_j \int_0^{2\pi} d\phi_j \sum_{i=1}^n V_{dip}(\vec{r}, \vec{r}_i, \phi_i)^2 \\ &= \frac{1}{2A^n} \left( \frac{qd}{4\pi\epsilon_r\epsilon_0} \right)^2 \sum_{i=1}^n \prod_{j=1}^n \iint_A dA_j \frac{(x - x_i)^2 + (y - y_i)^2}{((x - x_i)^2 + (y - y_i)^2 + h^2)^3} \end{aligned} \quad (S5)$$

Switching to polar coordinates and evaluating Eq. (S5) at the origin, we get

$$\sigma_{V_0}^2 = \left( \frac{qd}{4\pi\epsilon_r\epsilon_0} \right)^2 \frac{nr_0^2}{4h^2(h^2 + r_0^2)^2}, \quad (S6)$$



where  $r_0$  is the radius of the area  $A$  integrated over. Taking the derivative of Eq. (S2) with respect to a single direction and following the same procedure outlined above, one can calculate the RMS fluctuations in the electric field at the origin ( $F_0$ ). The result is

$$\sigma_{F_0}^2 = \left( \frac{qd}{4\pi\epsilon_r\epsilon_0} \right)^2 \frac{n(8h^6 + 8h^4r_0^2 + 12h^2r_0^4 + 3r_0^6)}{16h^4(h^2 + r_0^2)^4}. \quad (\text{S7})$$

It is now straight forward to calculate the dephasing of an EDSR qubit. The SD of the qubit's energy splitting is

$$\sigma_E = g\mu_B b_{\text{long}} \sigma_r = g\mu_B b_{\text{long}} \frac{e\sigma_{F_0}}{m^*\omega_0^2}, \quad (\text{S8})$$

where  $b_{\text{long}}$  is the longitudinal magnetic field gradient,  $\mu_B$  is the Bohr magneton and  $g$  is the electron g-factor. The last equality of Eq. (S8) comes from Eq. (S1). Inserting Eq. (S8) into Eq. (7) and simplifying, we arrive at

$$T_2^* = \frac{2\sqrt{2}}{g} \frac{m^*m_e\omega_0^2}{e^2b_{\text{long}}\sigma_{F_0}}. \quad (\text{S9})$$

Given  $b_{\text{long}} = .2 \frac{\text{mT}}{\text{nm}}$  [S1] and  $\omega_0 = 2 \text{ meV}/\hbar$ , along with all the noise parameters in Table I,  $T_2^* \approx 20 \mu\text{s}$ .

### III. PULSE OPTIMIZATION

Control pulses for elements of the universal gate set are created using QuTiP version 5.0.2 [S2, S3] and the Qutip quantum information processing package [S4]. The collection of pulses found with QuTiP are shown in Fig. S2. The

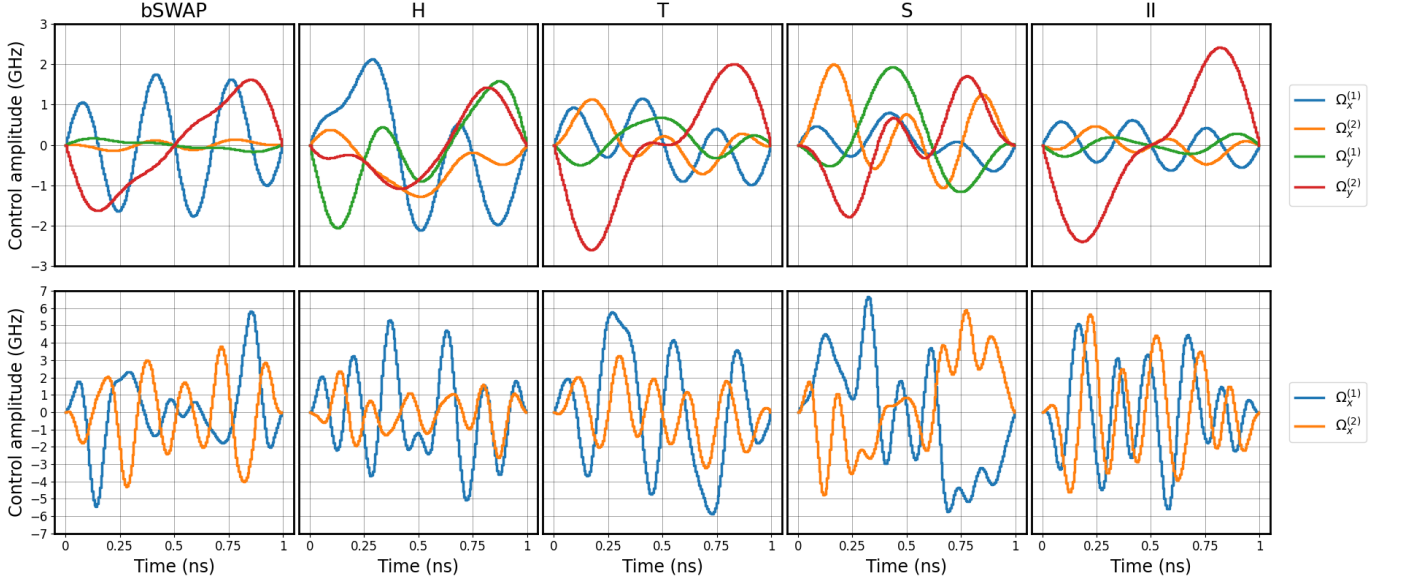


FIG. S2. GRAPE optimized pulse shapes. Upper half (lower half) corresponds to  $\frac{\omega_c}{2\pi} = 0$  (4.5) GHz and a maximum available bandwidth of 3 (10) GHz. The legend next to each half indicates what control parameters were used for the respective pulses.

exact code used to generate these pulses can be found in this paper's companion repository [S5], along with updated modules that should replace their predecessors in the standard QuTip-qtrl package. The module edits enable 1) a Fermi function envelope to GRAPE generated pulses and 2) a high frequency contribution to the cost function. Explicit details about how to run the code can be found in the repository's README.

---

[S1] J. Yoneda, K. Takeda, T. Otsuka, T. Nakajima, M. R. Delbecq, G. Allison, T. Honda, T. Kodera, S. Oda, Y. Hoshi, N. Usami, K. M. Itoh, and S. Tarucha, *Nature Nanotech.* **13**, 102 (2018).

- [S2] J. Johansson, P. Nation, and F. Nori, Computer Physics Communications **183**, 1760 (2012).
- [S3] QuTip Documentation, Version: 5.0.2 .
- [S4] QuTip-qtrl Documentation, Version: stable .
- [S5] Code Repository, GitHub .